





An Accreting Supermassive Black Hole Irradiating Molecular Gas in NGC 2110

David J. Rosario¹ , Aditya Togi^{2,3}, Leonard Burtscher⁴, Richard I. Davies⁵, Thomas T. Shimizu⁵ , and Dieter Lutz⁵ ¹Centre for Extragalactic Astronomy, Department of Physics, Durham University, South Road, Durham DH1 3LE, UK²St. Mary's University, San Antonio, TX, USA³University of Texas, San Antonio, TX, USA⁴Leiden Observatory, Leiden University, P.O. Box 9513, 2300 RA Leiden, The Netherlands⁵Max Planck Institut für Extraterrestrische Physik, Giessenbachstrasse 1, D-85748 Garching bei München, Germany

Received 2019 February 8; revised 2019 March 15; accepted 2019 March 22; published 2019 April 15

Abstract

The impact of active galactic nuclei (AGNs) on star formation has implications for our understanding of the relationships between supermassive black holes and their galaxies, as well as for the growth of galaxies over the history of the universe. We report on a high-resolution multiphase study of the nuclear environment in the nearby Seyfert galaxy NGC 2110 using the Atacama Large Millimeter/submillimeter Array, *Hubble* and *Spitzer Space Telescopes*, and the Very Large Telescope/SINFONI. We identify a region that is markedly weak in low-excitation CO 2 \rightarrow 1 emission from cold molecular gas, but appears to be filled with ionized and warm molecular gas, which indicates that the AGN is directly influencing the properties of the molecular material. Using multiple molecular gas tracers, we demonstrate that, despite the lack of CO line emission, the surface densities and kinematics of molecular gas vary smoothly across the region. Our results demonstrate that the influence of an AGN on star-forming gas can be quite localized. In contrast to widely held theoretical expectations, we find that molecular gas remains resilient to the glare of energetic AGN feedback.

Key words: galaxies: nuclei – galaxies: Seyfert – infrared: ISM – ISM: molecules – molecular processes – submillimeter: ISM

1. Introduction

Stars form exclusively in the cold, dense molecular interstellar medium (ISM; Kennicutt 1989; Bigiel et al. 2008). Active galactic nuclei (AGNs) alter the excitation and chemistry of cold molecular gas, an important pathway that can suppress future star formation in galaxies (Sternberg et al. 1994; Usero et al. 2004; Krips et al. 2008) and establish a coevolutionary connection between black hole and galaxy growth (Alexander & Hickox 2012; Kormendy & Ho 2013; Heckman & Best 2014). Molecular spectroscopy has uncovered indirect evidence that AGNs can alter central molecular gas, usually from the enhanced intensity of the rotational lines of the HCN and HCO⁺ molecules in active nuclei (Kohno et al. 2003, 2008; Usero et al. 2004; Krips et al. 2011; Izumi et al. 2013; García-Burillo et al. 2014; Imanishi et al. 2016; Querejeta et al. 2016). However, conditions unrelated to the AGN can also boost these lines, such as high gas densities, high molecular abundances, and infrared pumping (Sternberg et al. 1994; Izumi et al. 2013, 2016).

Here we present evidence for localized transformation of molecular gas through direct impact from the AGN's radiation field in the nearby Seyfert 2 galaxy NGC 2110 (luminosity distance $D_L = 34$ Mpc, $cz = 2335$ km s⁻¹). In Section 2, we present the various high-resolution and ancillary data sets used in this work, followed by an imaging and spectroscopic analysis, including a modeling of molecular lines, that reveals the interaction and its properties.

2. Observations and Data Preparation

Table 1 summarizes the multiwavelength data used for this study. Unless otherwise specified, we employed standard pipelines to reduce these data, adopting parameters recommended

by the respective observatories. The various images used in this work are brought together for context in Figure 1.

2.1. ALMA Spectroscopy

From the reduced Atacama Large Millimeter/submillimeter Array (ALMA) data set, we used CLEAN to generate a 1 mm continuum map and a CO 2 \rightarrow 1 cube with a velocity resolution of 5 km s⁻¹, both with a common restoring beam of 0".71 \times 0".45 (PA of -79°). We resampled these maps to 0".24 square spaxels for our final measurements.

We obtained a CO 2 \rightarrow 1 map by integrating the cube in velocity across a 900 km s⁻¹ window centered on the systemic velocity of the galaxy (Figure 1(a)). We also measured CO 2 \rightarrow 1 kinematics directly from the cube by fitting a single Gaussian to the line in each spaxel with an integrated S/N > 5, using the Python package LMFIT.⁶

2.2. Optical and NIR HST Imaging

We used narrowband images (FR680P15) covering the H α and [N II] $\lambda\lambda$ 6548, 6584 emission line complex from which we scaled and subtracted an associated line-free optical broadband image (F791W), to generate a pure emission line map of the circumnuclear region (Figure 1(a); Figure 3).

We produced a color map (Figure 1(c)) by dividing the F791W image by the deep near-infrared (NIR) image (F200N). The smooth stellar light profile of NGC 2110 makes the NIR image an ideal backdrop for the dust features that stand out in the optical. However, the nucleus of NGC 2110 emits continuum at 2 μ m from hot nuclear dust (>1000 K) that is invisible at optical wavelengths (Burtscher et al. 2015). This produces a nuclear red excess in the color map of the size of the point-spread function

⁶ <https://lmfit.github.io/lmfit-py/index.html>

Table 1
Summary of Observational Data Sets

Telescope/Instrument	Filter/Band	Program ID
ALMA	Band 6	2012.1.00474.S
<i>HST</i> /WFPC2	FR680P15	8610
<i>HST</i> /WFPC2	F791W	8610
<i>HST</i> /NICMOS (NIC3)	F200N	7869
VLT/SINFONI (AO)	<i>K</i>	086.B-0484(A)
VLT/SINFONI (AO)	<i>J</i>	060.A-9800(K)
<i>Spitzer</i> /IRS	SH+LH	AOR: 4851456

(PSF) of the NIR image (FWHM $\approx 0''.26$). This region of anomalous color is disregarded in our analysis.

2.3. VLT/SINFONI Integral Field Unit Spectroscopy

Using a custom pipeline, we reduced both SINFONI data sets to cubes with a plate scale of $0''.05$ to take full advantage of the resolution offered by adaptive optics (AO).

We used the *K*-band cube to measure the strength and kinematics of the H_2 1–0 S(1) line at $2.12 \mu\text{m}$, modeled in each spaxel as a single Gaussian with an underlying linear continuum. A telluric residual from the reduction, masked appropriately in these fits, prevented accurate line measurements in a few spaxels immediately around the continuum-bright nucleus. The apparent central hole in the H_2 S(1) maps of Figures 1(b) and 5 are the consequence of this: the measurements in those spaxels have been excluded from any analysis.

From the *J*-band cube, we assessed the spatial structure of the [Fe II] $1.25 \mu\text{m}$ emission line (Figure 3). We fit this line using the same procedure as the $2.12 \mu\text{m}$ H_2 S(1) line, but without the need to mask the central spaxels.

2.4. Image Registration and Astrometry

The ALMA images are astrometrically calibrated to the International Celestial Reference System with an accuracy ≈ 30 mas. We have adopted the VLA radio core as the coordinates of the nucleus (R.A.(J2000) = 5:52:11.379, decl.(J2000) = $-7:27:22.52$), and verified that it lies within 30 mas of the peak of the unresolved nuclear core at 1 mm.

The *Hubble Space Telescope* (*HST*) images have accurate relative astrometry, but their absolute astrometry is noticeably incorrect. We derived a simple shift correction to the astrometric frame of the optical and NIR continuum images based on the difference between the centroidal positions and the absolute *GAIA* positions of two stars that lie within $20''$ of the galaxy center. We visually verified that the peak of the NICMOS image lines up within 50 mas of the radio nuclear position after we applied these astrometric corrections.

We obtained NIR continuum maps directly from the SINFONI cubes, both of which show clear peaks. We registered the SINFONI cubes by tying the centroids of the continuum maps to the radio nuclear position. The relative astrometry of SINFONI across its small field of view (FoV) is accurate enough for our purposes.

2.5. Spitzer/IRS High-resolution Spectroscopy

We downloaded fully reduced, background-subtracted, optimally extracted mid-infrared (MIR) spectra of NGC 2110 from the CASSIS⁷ value-added database (Figure 2).

We measured the fluxes of the MIR molecular hydrogen (H_2) 0–0 rotational lines at $28.2 \mu\text{m}$ [S(0)], $17.0 \mu\text{m}$ [S(1)], and $12.3 \mu\text{m}$ [S(2)], modeling each line as the combination of a single Gaussian profile and an underlying linear continuum. The S(1) and S(2) lines are both well detected with signal-to-noise ratio (S/N) > 8 , while the S(0) line is marginally detected with an S/N ≈ 2 .

The spectra from CASSIS are extracted following the spatial profile of the nuclear point source. The S(1,2) lines from the Short-High module (FWHM of $3''.5$ – $6''$) are extracted over an area close to the SINFONI FoV, so aperture mismatch does not drastically affect our comparisons of these lines to the integrated H_2 1–0 line emission (Section 3.2). The PSF in the Long-High module at the S(0) line is considerably larger (FWHM of $9''$), and covers almost all of the detected CO emission seen in the ALMA maps.

3. Direct Evidence for AGN Feedback on Molecular Gas in NGC 2110

3.1. A Localized Lack of Cold Molecular Gas Emission

Figure 1(a) shows the ALMA CO $2 \rightarrow 1$ map in the center of NGC 2110. This emission is distributed in an inhomogeneous spiral pattern suggestive of a circumnuclear disk. Many of the bright arms of the CO disk are aligned with dark dust lanes seen in the *HST* color map (Figure 1(c)). For example, the brightest CO emission west of the nucleus is cospatial with the dusty spiral arm on the near side of the galaxy (e.g., Section 6 of Rosario et al. 2010). Bordering this arm, one finds a conspicuous lack of CO emission in an extended linear structure passing through the nucleus at PA $\approx -25^\circ$, particularly within a few arcseconds of the nucleus, where it bisects a region of high CO surface brightness, but it also extends to the SE and NW of the nucleus. Henceforth, we use the term “lacuna” to identify this feature.

The lacuna is well resolved, and therefore unlikely to arise from CO $2 \rightarrow 1$ line absorption against the nuclear millimeter continuum in the galaxy (Tremblay et al. 2016), which is dominated by the well-known radio jet (compare the blue contour in Figure 1(c) to the VLA 3.6 cm map in Figure 7 of Nagar et al. 1999). NGC 2110 does not display a well-defined bisymmetric pattern ($m = 2$; grand design spiral or stellar bar), so the separation of the two peaks of CO emission on either side of the lacuna cannot be easily attributed to stalling at an inner Lindblad resonance, as has been noted in some barred galaxies (Kenney et al. 1992).

An examination of other excited ISM phases reveals a more intimate connection to the lacuna. The $2.12 \mu\text{m}$ H_2 1–0 S(1) line, produced by hot excited molecular hydrogen, is located almost completely within the region (Figure 1(b)). A similar anticorrelation between hot and cold molecular phases has been noted in other systems (e.g., Davies et al. 2004, 2014; Mezcua et al. 2015; Espada et al. 2017). Over the CO $2 \rightarrow 1$ map in Figure 1(a), we have overlaid the contours from the $\text{H}\alpha$ + [N II] emission line map. Studies have established this gas is ionized either by photoionization from nuclear ultraviolet and X-ray

⁷ <http://cassis.sirtf.com/>

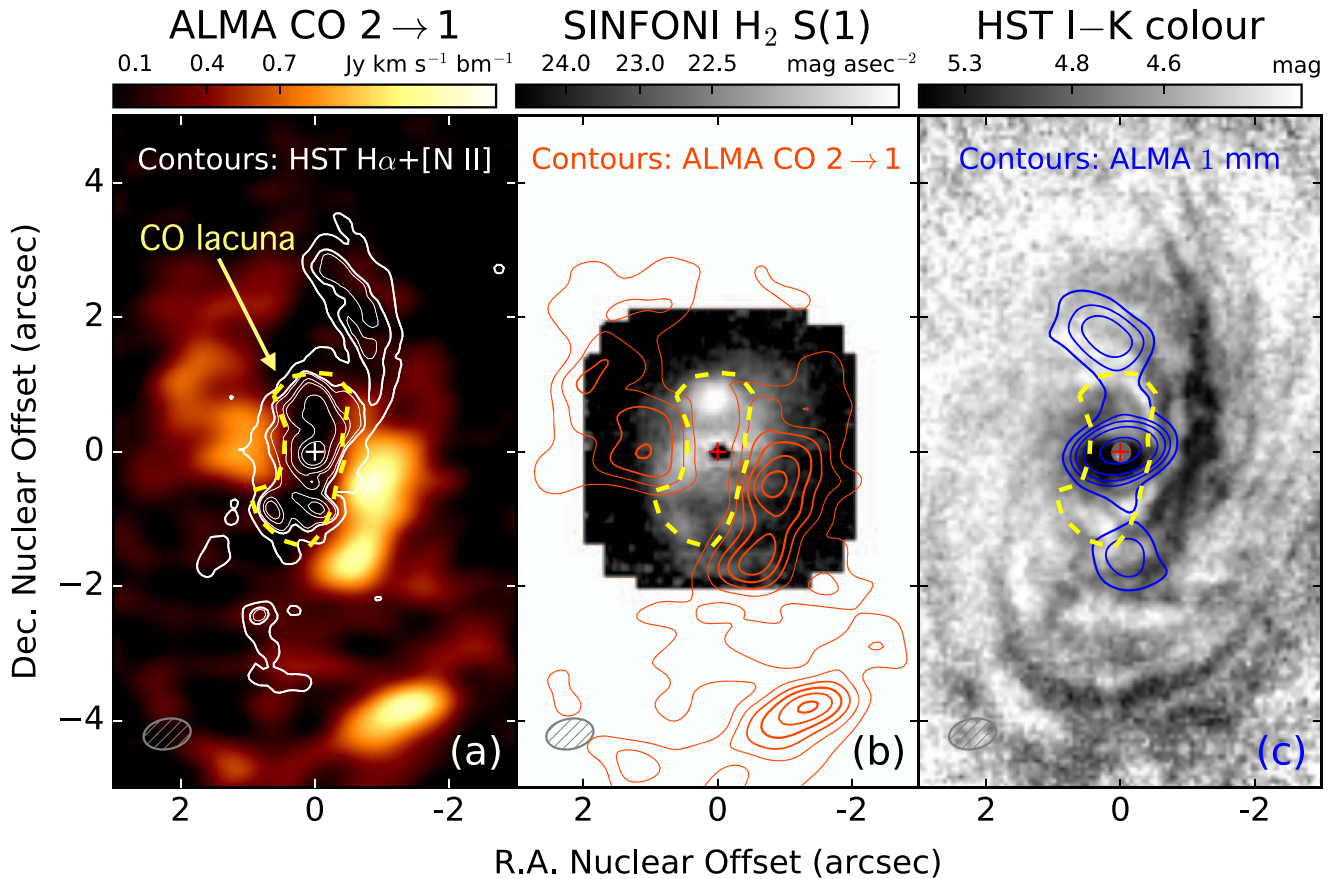


Figure 1. Multiwavelength view of the central region of NGC 2110. North is up and east to the left. In all three panels, the nucleus is marked with a cross, the ALMA synthesized beam is shown as a gray ellipse, and the region of CO lacuna (see Section 3.1) is demarcated with a dashed yellow polygon. The thickness of contour lines, when shown, are used to emphasize shape rather than surface brightness. Panel (a): ALMA CO 2 \rightarrow 1 line map. Contours are from the *HST* map of the $H\alpha$ + [N II] emission line complex at 6560 Å, smoothed to match the angular resolution of the ALMA data. Panel (b): a map of the H_2 1–0 S(1) line at 2.12 μm from VLT/SINFONI. The contours of the ALMA CO 2 \rightarrow 1 emission from panel (a) are overlaid. Panel (c): a map of the ratio of F791W (optical) and F200N (near-infrared) images from *HST*, which emphasizes dust absorption as dark features. The dust map is inaccurate at the nucleus (masked by a small white circle) because of excess near-infrared emission from hot dust around the AGN (see Section 2.2 for details). The blue contours show the shape of the ALMA 1 mm continuum, which traces the bipolar radio jet in this AGN.

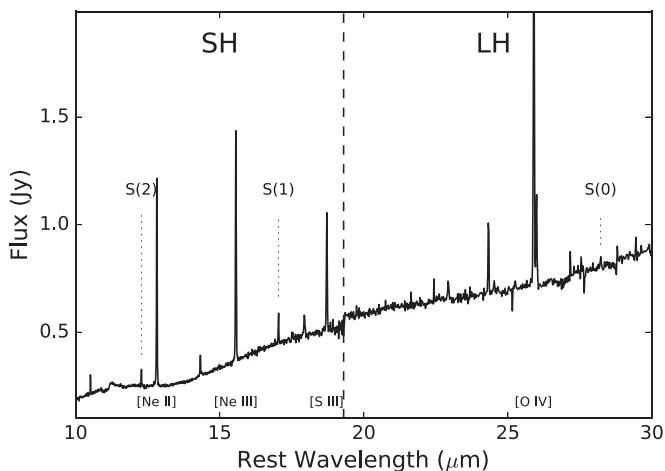


Figure 2. Complete high-resolution *Spitzer*/IRS spectrum of NGC 2110 including both short (SH) and long (LH) spectral segments. Measurable H_2 0–0 rotational emission lines are labeled with dotted line markers; prominent ionized gas emission lines are also identified.

light, or via shocks from a fast wind with velocities of several 100 km s^{-1} (Ferruit et al. 1999; Rosario et al. 2010; Schnorr-Müller et al. 2014). The narrow bipolar shape may be due to the

anisotropic illumination of the circumnuclear disk by the AGN (e.g., Figure 7 of Rosario et al. 2010).

Figure 1(a) reveals a close spatial association between the CO lacuna and the AGN-ionized emission line gas. The two structures are highly cospatial, and the CO emission is noticeably weaker along the axis of the ionized gas. Within an arcsecond of the nucleus, the inner edges of the lacuna are defined by bright CO features that mirror the outer edges of the emission line region.

The cold, dusty gas that produces CO 2 \rightarrow 1 could potentially shape the observed optical emission line structure through selective extinction, resulting in an apparent anticorrelation between the two phases. We test this by examining a map of the 1.25 μm [Fe II] line, which is also excited by the AGN, but is less extinguished by dust than $H\alpha$ + [N II]. The similarity of the two maps (Figure 3) confirms that the intrinsic structure of the AGN-ionized region is accurately represented by the contours in Figure 1(a). NIR hydrogen recombination lines, such as $\text{Br}\gamma$ at 2.17 μm , also share the same basic size and structure (Diniz et al. 2015).

Interestingly, the *HST* color map (Figure 1(c)) also reveals considerable dusty gas within the lacuna that is not visible in CO 2 \rightarrow 1. At larger nuclear distances, the ionized gas traces

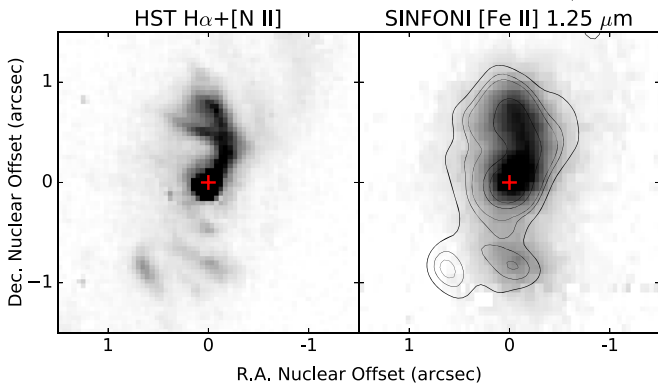


Figure 3. Comparison of emission line maps in the optical (left; the *HST* $H\alpha$ +[N II] complex at full resolution) and the near-infrared (right; the [Fe II] $1.25 \mu\text{m}$ line in the *J* band from VLT/SINFONI). To highlight their similarity, we overlay the contours of the *HST* map in the right panel after matching it to the angular resolution of the SINFONI map. The contour levels are unequally spaced; the lowest to highest contour levels span 9×10^{-19} – $10^{-17} \text{ W m}^{-2} \text{ arcsec}^{-2}$. The nucleus is marked with a cross in both panels; north is to the top, and east is to the left.

spiral features visible in the *HST* dust map, yet the CO emission here also remains weak.

3.2. Associated Enhancement in Warm Molecular Gas Emission

Fundamental insight into the nature of the lacuna comes from the modeling of the molecular line sequence of warm H_2 from *Spitzer*/IRS spectroscopy.

In the complex environment of a galaxy nucleus, a few discrete temperature components do not adequately describe the excitation of H_2 gas. Adopting the approach of Togi & Smith (2016), we assume a uniform power-law model of the distribution of H_2 temperatures, with the form $dN \propto T^{-n} dT$, where dN is the column density of molecules in the temperature range $T - T + dT$. The two free parameters are the power-law index n and the lower temperature T_ℓ , respectively. The upper temperature of the distribution is fixed at 50,000 K, though realistically the fraction of molecular mass with temperatures greater than a few thousand Kelvin is negligible.

Figure 4 shows an H_2 excitation diagram that illustrates the constraints offered by the measured H_2 rotational lines (including limits), and the associated uncertainties on the power-law index. In the diagram, we plot the column density of molecules populated by the upper level of a transition (N_u) divided by its statistical weight (g_u) against the energy level of the transition (E_u). We follow the custom of normalizing the excitation to the 0–0 S(1) line (Togi & Smith 2016). Extrapolating the power-law model to temperatures $>1000 \text{ K}$ gives an estimate of the flux of the 1–0 S(1) line at $2.12 \mu\text{m}$, which also serves as a constraint. The hot H_2 gas that emits this line is a very small fraction (typically $<0.1\%$) of the total molecular mass (M_{mol}); therefore, this extrapolation is strictly contingent on the continuity of the power-law distribution of temperatures beyond several hundred Kelvin. The similarity of the rotational and vibrational temperatures derived from the NIR H_2 lines implies that even the hot molecular material is in thermal equilibrium (Diniz et al. 2015), lending some support to this assumption.

Fixing the model to the formally measured flux of the S(0) line, we obtain $n = 4.48$ (black line in Figure 4). This value is toward the upper end of the range found among star-forming

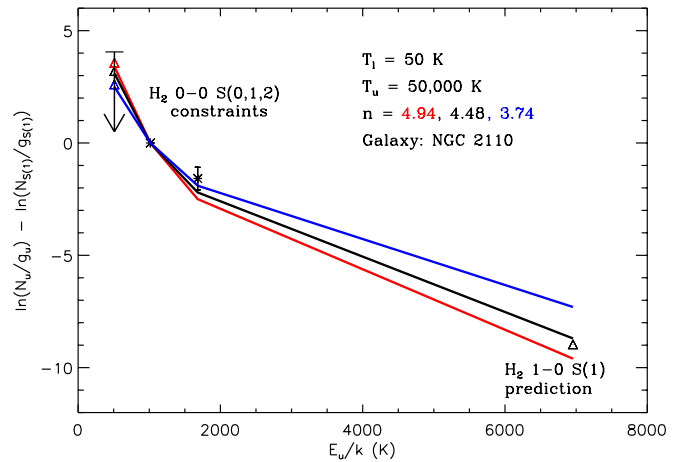


Figure 4. Excitation diagram of H_2 showing our power-law fit to the mid-infrared 0–0 rotational line strengths and the extrapolation of the models to the 1–0 S(1) line at $2.12 \mu\text{m}$. Colored lines correspond to models with different power-law indices (n) as shown in the key. The downward arrow is the 3σ upper limit on the 0–0 S(0) constraint. See Section 3.2 for more details.

galaxies in the *Spitzer* Infrared Nearby Galaxies Survey (Togi & Smith 2016). Such a shallow temperature distribution arises from a higher mass fraction of warm H_2 than typically found in galaxy environments. Considering temperatures as low as 50 K to include the cold component that emits $\text{CO } 2 \rightarrow 1$, we calculate $M_{\text{mol}} = 2.5 \times 10^8 M_\odot$, including the contribution of helium and heavier elements

From Figure 4, it is clear that the adopted strength of the 0–0 S(0) line strongly influences the determination of n , and therefore the final estimate of M_{mol} . A nominal uncertainty of 0.3 dex for the line flux implies a mass in the range of $(0.9\text{--}4.6) \times 10^8 M_\odot$. The estimated mass is correlated with n : a larger proportion of molecules at high temperatures (lower n) results in a lower estimate of M_{mol} . In addition, the S(0) constraint should be formally considered an upper limit because the aperture used for the measurement of this line covers a substantially larger area than the lacuna itself; the arrow in Figure 4 shows the equivalent 3σ limit on the line. Therefore, the molecular mass associated with the lacuna could be even smaller than the range calculated above.

However, in this regard, the $2.12 \mu\text{m}$ 1–0 S(1) provides a measure of discriminatory power. Figure 4 shows that a single power-law model tied to the formal flux of the S(0) line can reproduce the fluxes measured in all four H_2 lines quite well. This suggests that the S(0) line flux is not very extended, but mostly concentrated within the lacuna and its immediate surroundings.

We can also estimate the total molecular gas mass directly from the $\text{CO } 2 \rightarrow 1$ line over the same region ($F_{\text{CO}} = 13 \text{ Jy km s}^{-1}$ from a $4''$ circular aperture centered on the nucleus). Following Solomon & Vanden Bout (2005),

$$M_{\text{mol,CO}} = \frac{3.25 \times 10^7 R_{12} \alpha_{\text{CO}} F_{\text{CO}} D_L^2}{(1+z) \times (230.54 \text{ GHz})^2} M_\odot, \quad (1)$$

assuming a certain CO-to- H_2 conversion factor (α_{CO}) and a CO $1 \rightarrow 0$ to CO $2 \rightarrow 1$ brightness temperature ratio (R_{12}). Taking $R_{12} = 1.4$ and α_{CO} in the range of 1.5–3, consistent with observations of the centers of nearby galaxies (Sandstrom et al. 2013), we obtain $M_{\text{mol,CO}} \approx (2\text{--}4) \times 10^7 M_\odot$. This is considerably lower than M_{mol} estimated from the MIR H_2 lines.

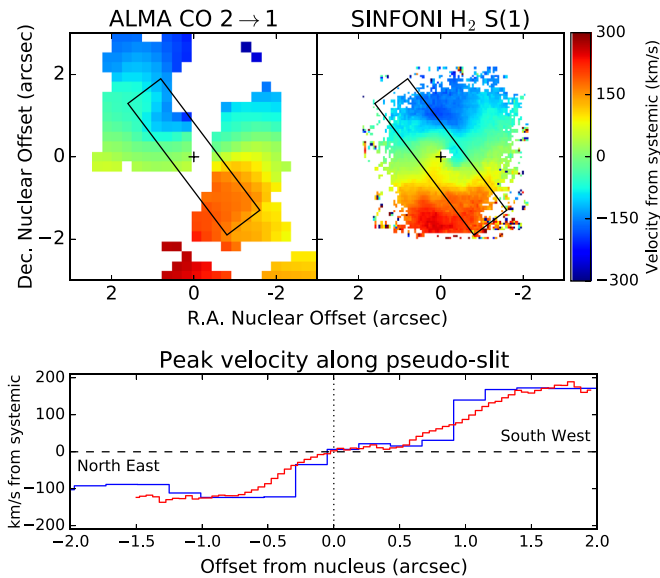


Figure 5. Top: peak systemic velocity offset of the CO $2 \rightarrow 1$ line (left) and the $2.12 \mu\text{m}$ H₂ 1–0 S(1) line (right) from ALMA and SINFONI data cubes. Bottom: velocity curves extracted from the same simulated long-slit aperture (the black rectangle in both top panels) from the CO (blue) and H₂ (red) data sets. Velocity errors, in the range of 2–10 km s^{−1}, are excluded for visual purposes. While the distributions of the cold and warm molecular gas are different, they share the same velocity field.

We postulate that the molecular mass invisible in CO $2 \rightarrow 1$ has been heated beyond the temperature at which it efficiently emits low-order CO lines, and this material is concentrated in the lacuna and shares the spatial distribution of the NIR H₂ S(1) line, a circular region of 0.34 kpc^2 . From the difference $M_{\text{mol}} - M_{\text{mol,CO}} \approx 2.2 \times 10^8 M_{\odot}$, we infer a molecular gas surface density of $650 M_{\odot} \text{ pc}^{-2}$. If we treat the S(0) line as a formal limit, and take $M_{\text{mol}} \approx 9 \times 10^7 M_{\odot}$, at the low end of the estimated range, the surface density drops to $180 M_{\odot} \text{ pc}^{-2}$. These calculations may be compared to the molecular gas surface density of $200\text{--}350 M_{\odot} \text{ pc}^{-2}$ inferred using Equation (1) in the bright CO knots around the edges of the lacuna.

The similarity of these two estimates, certainly within the systematic uncertainties of our modeling, suggests that the central molecular disk extends into the lacuna, despite its apparent CO deficiency.

Additional support comes from the comparison of the two-dimensional velocity fields of the CO $2 \rightarrow 1$ line and the H₂ 1–0 S(1) line (Figure 5). Despite differences in the temperature and excitation of these molecular species, both lines independently trace an inclined rotating disk with the same strong kinematic asymmetry, and noncircular motions as have been found previously from ionized gas studies (González Delgado et al. 2002; Ferruit et al. 2004; Schnorr-Müller et al. 2014; Diniz et al. 2015). From the continuity in the rotation fields of the cold and warm molecular gas, we infer that these two phases are connected and share the same circumnuclear dynamics.

3.3. AGN Feedback Suppresses CO $2 \rightarrow 1$ Emission

Based on the evidence developed above, the most likely explanation for the CO lacuna is that the energy liberated by the central AGN is directly influencing the molecular gas within the region and actively suppressing the emission of the CO $2 \rightarrow 1$ line. This “AGN feedback” can proceed in two

possible ways. Strong far-ultraviolet and X-ray radiation from the AGN penetrates past the ionized outer layers of dense clouds in the lacuna, heating the molecular gas within. This alters its chemistry, while photoexcitation and dissociation of CO suppresses the emission of the CO $2 \rightarrow 1$ line. Alternatively, slow shocks ($\lesssim 50 \text{ km s}^{-1}$) arising from the interaction between molecular gas and an AGN wind or radio jet depletes CO while boosting the emission of the warm molecular hydrogen lines. The molecular gas diagnostics currently available do not strongly discriminate between these mechanisms. The relative strengths of the rotational and rovibrational H₂ lines (Rodríguez-Ardila et al. 2005; Diniz et al. 2015) can be achieved with models that feature either shock or X-ray excitation (Maloney et al. 1996; Rigopoulou et al. 2002; Flower & Pineau Des Forêts 2010).

However, the entire optical and NIR line spectrum of NGC 2110, including the warm molecular lines, can be self-consistently reproduced by photoionization of metal-rich dusty gas ($\approx 2 \times$ the solar metal abundance) by a nuclear source with the known power of the AGN (Rosario et al. 2010; Dors et al. 2012). In light of this, the close relationship between the structure of the ionized gas, the warm H₂, and the CO lacuna supports radiative feedback as the principal cause for the transformation of the molecular gas.




Regardless of the primary process that suppresses the CO emission, our study concludes that an AGN can directly influence the local emissive and thermal properties of circumnuclear molecular gas. This is the first time such a strong association has been noted with such clarity. Querejeta et al. (2016) have reported a similar connection in M51, though the conclusion is limited by the resolution of their CO data. In NGC 1068, the archetypical local Seyfert, the CO emission appears to be decoupled from its well-known ionization cone (e.g., Figure 6 in García-Burillo et al. 2014). NGC 5643 may show some evidence in an extended arm of CO emission intersecting the ionization cone (e.g., Figure 1 in Alonso-Herrero et al. 2018).

An important corollary worth highlighting is that such interaction could be quite localized. There is considerable molecular material in the vicinity of the nucleus of NGC 2110, which remains free of any obvious nuclear impact. Even within the lacuna, we find that molecular material can remain resilient to the mechanical effects of radiation pressure or AGN winds. This has important implications for the role of AGN feedback in regulating and suppressing star formation in galaxies. NGC 2110 will serve as a valuable laboratory to explore this key process that underpins our modern theoretical view of galaxy evolution.

D.R. acknowledges the support of the Science and Technology Facilities Council (STFC) through grant ST/P000541/1. ALMA is a partnership of ESO (representing its member states), NSF (USA) and NINS (Japan), together with NRC (Canada), MOST and ASIAA (Taiwan), and KASI (Republic of Korea), in cooperation with the Republic of Chile. Based on observations collected at the European Organisation for Astronomical Research in the Southern Hemisphere; with the NASA/ESA *Hubble Space Telescope*, obtained from the data archive at the Space Telescope Science Institute, which is operated by the Association of Universities for Research in Astronomy, Inc. under NASA contract NAS 5-26555; and with the *Spitzer Space Telescope*, which is operated by the Jet

Propulsion Laboratory, California Institute of Technology under a contract with NASA.

ORCID iDs

David J. Rosario  <https://orcid.org/0000-0002-0001-3587>
 Thomas T. Shimizu  <https://orcid.org/0000-0002-2125-4670>
 Dieter Lutz  <https://orcid.org/0000-0003-0291-9582>

References

- Alexander, D. M., & Hickox, R. C. 2012, *NewAR*, 56, 93
 Alonso-Herrero, A., Pereira-Santaella, M., García-Burillo, S., et al. 2018, *ApJ*, 859, 144
 Bigiel, F., Leroy, A., Walter, F., et al. 2008, *AJ*, 136, 2846
 Burtscher, L., Orban de Xivry, G., Davies, R. I., et al. 2015, *A&A*, 578, A47
 Davies, R. I., Maciejewski, W., Hicks, E. K. S., et al. 2014, *ApJ*, 792, 101
 Davies, R. I., Tacconi, L. J., & Genzel, R. 2004, *ApJ*, 602, 148
 Diniz, M. R., Riffel, R. A., Storchi-Bergmann, T., & Winge, C. 2015, *MNRAS*, 453, 1727
 Dors, O. L., Jr., Riffel, R. A., Cardaci, M. V., et al. 2012, *MNRAS*, 422, 252
 Espada, D., Matsushita, S., Miura, R. E., et al. 2017, *ApJ*, 843, 136
 Ferruit, P., Mundell, C. G., Nagar, N. M., et al. 2004, *MNRAS*, 352, 1180
 Ferruit, P., Wilson, A. S., Whittle, M., et al. 1999, *ApJ*, 523, 147
 Flower, D. R., & Pineau Des Forêts, G. 2010, *MNRAS*, 406, 1745
 García-Burillo, S., Combes, F., Usero, A., et al. 2014, *A&A*, 567, A125
 González Delgado, R. M., Arribas, S., Pérez, E., & Heckman, T. 2002, *ApJ*, 579, 188
 Heckman, T. M., & Best, P. N. 2014, *ARA&A*, 52, 589
 Imanishi, M., Nakanishi, K., & Izumi, T. 2016, *AJ*, 152, 218
 Izumi, T., Kohno, K., Aalto, S., et al. 2016, *ApJ*, 818, 42
 Izumi, T., Kohno, K., Martín, S., et al. 2013, *PASJ*, 65, 100
 Kenney, J. D. P., Wilson, C. D., Scoville, N. Z., Devereux, N. A., & Young, J. S. 1992, *ApJL*, 395, L79
 Kennicutt, R. C., Jr. 1989, *ApJ*, 344, 685
 Kohno, K., Ishizuki, S., Matsushita, S., Vila-Vilaró, B., & Kawabe, R. 2003, *PASJ*, 55, L1
 Kohno, K., Nakanishi, K., Tosaki, T., et al. 2008, *Ap&SS*, 313, 279
 Kormendy, J., & Ho, L. C. 2013, *ARA&A*, 51, 511
 Krips, M., Martín, S., Eckart, A., et al. 2011, *ApJ*, 736, 37
 Krips, M., Neri, R., García-Burillo, S., et al. 2008, *ApJ*, 677, 262
 Maloney, P. R., Hollenbach, D. J., & Tielens, A. G. G. M. 1996, *ApJ*, 466, 561
 Mezcua, M., Prieto, M. A., Fernández-Ontiveros, J. A., et al. 2015, *MNRAS*, 452, 4128
 Nagar, N. M., Wilson, A. S., Mulchaey, J. S., & Gallimore, J. F. 1999, *ApJS*, 120, 209
 Querejeta, M., Schinnerer, E., García-Burillo, S., et al. 2016, *A&A*, 593, A118
 Rigopoulou, D., Kunze, D., Lutz, D., Genzel, R., & Moorwood, A. F. M. 2002, *A&A*, 389, 374
 Rodríguez-Ardila, A., Riffel, R., & Pastoriza, M. G. 2005, *MNRAS*, 364, 1041
 Rosario, D. J., Whittle, M., Nelson, C. H., & Wilson, A. S. 2010, *MNRAS*, 408, 565
 Sandstrom, K. M., Leroy, A. K., Walter, F., et al. 2013, *ApJ*, 777, 5
 Schnorr-Müller, A., Storchi-Bergmann, T., Nagar, N. M., et al. 2014, *MNRAS*, 437, 1708
 Solomon, P. M., & Vanden Bout, P. A. 2005, *ARA&A*, 43, 677
 Sternberg, A., Genzel, R., & Tacconi, L. 1994, *ApJL*, 436, L131
 Togi, A., & Smith, J. D. T. 2016, *ApJ*, 830, 18
 Tremblay, G. R., Oonk, J. B. R., Combes, F., et al. 2016, *Natur*, 534, 218
 Usero, A., García-Burillo, S., Fuente, A., Martín-Pintado, J., & Rodríguez-Fernández, N. J. 2004, *A&A*, 419, 897